2026 ASEE ANNUAL CONFERENCE June 21–24, 2026 | Charlotte Convention Center, NC

Host Sponsor UNC Charlotte

Paper ID #52305

Interdisciplinary Learning Design: Machine Learning Assisted Brewster Angle Microscopy Image Analysis for Biodegradable Poly(caprolactone)-based Langmuir Films

Yeonhyang Kim, Central Michigan University
Hiruni Kamali Pallage, Centre College

Hiruni Pallage is an Assistant Professor of Mathematics at Centre College. She earned her Ph.D. in Mathematics from Central Michigan University, where her research focused on interpolation and data-driven methods for improving brain imaging techniques.

Her research lies in applied and interdisciplinary mathematics, including image processing, data analysis, and mathematical modeling, with applications in neuroscience and materials science. Her work spans topics such as interpolation on spherical domains, dynamical sampling, and image-based analysis of polymer morphologies, and has been published in journals including the Journal of Mathematical Analysis and Applications and Colloids and Surfaces A.

Dr. Pallage is committed to integrating research into undergraduate education. At Centre College, she teaches courses in calculus, linear algebra, operations research, and advanced interpolation methods, emphasizing mathematical modeling, computation, and real-world applications. She has presented her work at national conferences, including invited sessions at the Joint Mathematics Meetings.

Linxi Zhang, Central Michigan University
Grant Wang, University of Michigan
Prof. Bingbing Li, Central Michigan University

Prof. Bingbing Li (the corresponding author), the Department of Chemistry and Biochemistry, Central Michigan University. Dr. Li is a Professor and Chair of Chemistry and Biochemistry at Central Michigan University. Address: Department of Chemistry and Biochemistry, Central Michigan University, Mt Pleasant, MI 48859, USA. Corresponding author email: li3b@cmich.edu

Interdisciplinary Learning Design: Machine Learning Assisted Brewster Angle Microscopy Image Analysis for Biodegradable Poly(ε-caprolactone) -based Langmuir Films

Yeon H. Kim[⊥,a], Hiruni K. Pallage[⊥, a, c], Linxi Zhang[⊥, b], Grant Wang[d], Bingbing Li[e,*]

[a] *Department of Mathematics, Central Michigan University, Mt Pleasant, MI 48859, USA*
[b] *Department of Computer Science, Central Michigan University, Mt Pleasant, MI 48859, USA*
[c] *Department of Mathematics, Centre College, Danville, KY 40422, USA*
[d] *Department of Electrical and Computer Engineering, University of Michigan, Ann Arbor, MI 48109, USA*
[e] *Department of Chemistry and Biochemistry, Central Michigan University, Mt Pleasant, MI 48859, USA.*

[⊥]Equal contribution
*Corresponding author email: li3b@cmich.edu

Abstract: Interdisciplinary learning and collaboration skills have become critically important in the age of artificial intelligence. In this study, a team spanning physical chemistry and polymer sciences, mathematics, as well as computer science and engineering was formed to explore the applications of advanced machine learning (ML) algorithms in analyzing Brewster angle microscopy (BAM) images. While ML techniques have gained significant attention for microscopy image analysis, this study represents a pioneering effort to harness their power for analyzing BAM images. The BAM technique is one of the most effective methods for *in-situ* visualizing the surface morphology of quasi-two-dimensional (2D) condensed phases formed at the air/water (A/W) interface. BAM's real-time imaging capability arises from the differences in refractive index among the gaseous (G), liquid-expanded (LE), liquid-condensed (LC), and solid phases of the Langmuir film formed at the A/W interface. This paper highlights the design framework and research outcomes of three modules: (a) crystallization and phase separation of biodegradable poly(ε-caprolactone) (PCL)/oligomeric polystyrene (o-PS)-based binary blends at

the A/W interface; (b) advanced ML workflows for denoising and enhancing BAM images using a generative AI–based deep learning framework. The workflow leverages Python and PyTorch/TensorFlow on CPUs or GPUs to accelerate model training and improve overall efficiency, and (c) segmentation and quantitative analysis workflow using MATLAB for raw and ML-processed images to identify, refine, and measure the phase-separated domains.

Introduction

Langmuir monolayers are usually formed by insoluble amphiphilic molecules with a hydrophilic headgroup that anchors the molecule at the water surface and a hydrophobic tail that prevents it from dissolving into the subphase. Upon spreading, amphiphilic molecules can rapidly occupy the available surface area and organize themselves at the Air/Water (A/W) interface to minimize their free energy. A well-ordered, monolayer-thick film thus formed during compression is known as a Langmuir monolayer. In contrast, the term Langmuir films encompasses both monolayers and multilayer structures formed at the A/W interface. Among various *in-situ* characterization methods for studying Langmuir films [1], BAM is particularly useful for monitoring the *in-situ* phase behavior of Langmuir films. This non-invasive imaging technique enables real-time observation of domain formation and growth, offering detailed insights into the texture, size, homogeneity, and other *in-situ* morphological features of the Langmuir film that cannot be obtained otherwise [2-7].

For instance, BAM technology has been heavily used to study the phase behavior of biodegradable poly(ε-caprolactone) (PCL) and PCL-based polymer blends at the A/W interface [2-7]. These previous studies have focused on the crystallization of neat PCL Langmuir films [4], the influence of molecular weight on PCL crystallization [5], the effect of surface pressure on

PCL crystallization under quasi-static conditions [6], and the crystallization and phase-separation behavior of various PCL-based mixed Langmuir films [2,3,7]. Cross all these studies, BAM technology was utilized simultaneously with surface pressure-area ($\prod$-A) measurements for capturing the nucleation and growth of PCL crystals, as well as the morphology evolution of phase separated PCL-based blends.

Despite its advantage as a non-invasive technique for visualizing phase transitions in Langmuir films, BAM technology is fundamentally constrained by its optical configuration. These limitations include the pixel size of the digital camera and the numerical aperture (N.A.) of its optical components. The pixel size determines the smallest detectable features in the image, while the numerical aperture determines the system's ability to resolve fine spatial details. These limitations often result in image distortion and insufficient resolution, which, especially the latter, pose significant barriers to the quantitative analysis of material's phase transition properties in quasi-2D film geometries. With the rapid development of machine learning (ML) techniques, the current study focuses on exploring the application of a generative deep learning-based image enhancement approach derived from Real-ESRGAN [8] to address the resolution and contrast limitations inherent to BAM images. The pretrained model is applied in an inference-focus manner to suppress background noise, enhance contrast, and improve domain boundary visibility, thereby preparing BAM images for subsequent quantitative domain analysis using MATLAB-based segmentation tools.

Besides the pioneering effort of using Real-ESRGAN to improve the resolution of BAM images, this project also aims to achieve several additional learning objectives: (1) gaining hands-on experience with generative AI models for microscopy image processing, including model selection and interpretation of outputs; (2) strengthening data analysis skills (e.g., MATLAB toolboxes) of all participants for future projects involving advanced image analysis; (3) developing a modular research workflow that supports interdisciplinary collaboration by removing domain-knowledge barriers; and (4) building AI-enabled research capacity across different participating disciplines.

To conduct this study, an interdisciplinary team was formed that included three faculty members from chemistry, mathematics, and computer science; a recent mathematics PhD graduate who had accepted an assistant professor position in another institution; and an undergraduate student. The team was assembled to leverage diverse expertise and different levels of experience. Even though the project was not implemented through a formal course, it provided faculty and student participants with valuable learning opportunities to engage in technologies that would otherwise have been difficult for them to access. Chemistry faculty interpreted microscopic data and provided the domain knowledge needed to understand the polymer blend films. Mathematics participants carried out image preprocessing and feature extraction tasks. Computer science and computer engineering participants worked on machine learning models and associated coding tasks. The project was organized into three distinct learning modules, outlined as follows.

In Module I, BAM imaging principle was first introduced to students and faculty in mathematics, computer science, and engineering disciplines to highlight the technology's limitations and spark interest in the field. Experimental methods carried out for monitoring the Langmuir films of PCL/oligomeric polystyrene (o-PS)-based binary blends were also introduced. It should be noted that the surface morphology of PCL/o-PS mixed monolayers exhibits substantial complexity as a function of blend composition and surface pressure during a dynamic compression process. Current study represents the initial attempt in ML-assisted BAM image analysis by focusing only on two representative PCL/o-PS blends with PS mole fractions (X_{PS}) of 0.68 and 0.77, respectively.

Module II focuses on advanced machine learning workflows for denoising and enhancing BAM images using a Real-ESRGAN-based generative deep learning framework. This method was selected due to its strong performance in restoring fine spatial details and suppressing complex noise patterns in microscopic images and other real-world imaging applications. The workflow is implemented in Python using PyTorch/TensorFlow and can be executed on CPU or GPU platforms to enable efficient model deployment and image processing. A pretrained model is applied in an inference-only manner to enhance contrast, suppress noise, and improve domain boundary visibility in BAM images, providing improved input quality for subsequent segmentation and quantitative analysis.

Module III focuses on the segmentation and quantitative analysis workflow using MATLAB to identify, refine, and measure phase-separated domains. A comparative study of raw and Real-ESRGAN-processed images for the two BAM images sets was carried out to explore the impact of the chosen algorithm on domain identification and measurement.

In this study, two sets of BAM images corresponding to $X_{PS} \approx 0.68$ and 0.77 mixed Langmuir films were chosen due to their distinct surface morphologies. The first set with $X_{PS} \sim 0.68$ displays predominantly optically uniform domains, while the second set captured for a mixed film with $X_{PS} \sim 0.77$ contains visible small secondary bright domains with optically heterogeneous surface morphologies. Overall, the Real-ESRGAN algorithm shows promise for preparing BAM images for segmentation analysis, although the visual quality of the processed images varies with the complexity of the surface morphology. For instance, the algorithm performs reasonably well for BAM images with optically uniform domains (e.g., $X_{PS} \sim 0.68$

samples) despite the tendency to overly average pixel intensity. On the other hand, for segmentation analysis performed in MATLAB, the results indicate that processed images offer clear advantages over raw images. For all images regardless of their optical complexity, the processed images enable the identification and isolation of a greater number of smaller domains, improving the measurement accuracy for both domain-size and area. With that said, even though the Real-ESRGAN algorithm does not effectively enhance the visual details of images containing optically complex 3D domains (e.g., X_{PS} ~ 0.77 samples), it still produces more reliable segmentations that support domain measurement. Looking forward, to improving visual image quality, particularly for BAM images with pronounced 3D domain structure and complex optical heterogeneity, alternative ML algorithms will likely be required.

Module I. BAM Study of PCL/oligomeric PS Mixed Langmuir Films

Materials and Methods. Oligomeric PS (weight average molar mass, M_w=740 g·mol^{-1}; polydispersity index, M_w/M_n = 1.06) and PCL (M_w = 10 kg·mol^{-1}; M_w/M_n = 1.25) were purchased from Polymer Source, Inc. and were used without further purification. A Hamilton gas-tight glass syringe was used to spread the PCL/o-PS blends solution (~ 0.5 mg·g^{-1}, chloroform, HPLC grade) onto the surface of ultrapure water (18.2 MΩ, Milli-Q Gradient A-10, Millipore, <5 ppb organic impurities) in a standard Langmuir trough (500 cm^2, 601BAM, Nima Technology). The spreading solvent was allowed to evaporate for ~20 minutes before isotherm measurements using a Wilhelmy plate technique. Brewster angle microscopy (BAM) (MiniBAM, NanoFilm Technologie GmbH, Linear resolution of at least 20 μm) studies were carried out simultaneously during the isotherm measurements [2-7]. BAM micrographs were taken with a CCD camera. The BAM images presented in this paper are 1.2×1.6 mm^2 in size unless specifically noted. The Langmuir trough and BAM were maintained at 22.5 °C in a Plexiglas box with a relative humidity of 70-75% on a floating optical table to minimize vibrations.

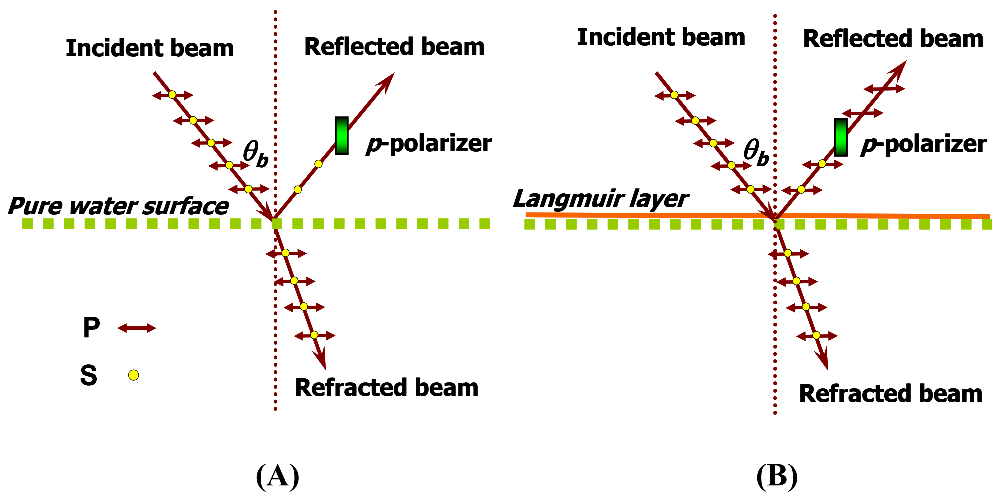

Figure 1. Laser-beam diagrams for BAM show (A) a pure water surface and (B) a film-covered surface. Arrows mark *p*-polarized light and small circles mark *s*-polarized light (perpendicular to the page). The incident beam is set to the Brewster angle of pure water. A *p*-polarizer is placed in the reflected beam to remove any remaining *s*-polarized light before it reaches the detector [9].

BAM Experimental Configuration. A beam diagram for BAM is shown in **Figure 1** [9]. When light passes through a medium with a lower refractive index (e.g., air, RI ≈ 1.00) into a medium with a higher refractive index (e.g., water respective to air, RI ≈ 1.33), some fraction of *p*-polarized light will be reflected at all incident angles except at Brewster's angle (θ_B). For Mini-BAM instrument, the angle of the incident light is set to Brewster's angle (θ_B = 53.1° for water) for the A/W interface, which minimizes the reflection of *p*-polarized light from a pure water surface as shown in **Figure 1A**. However, for a film-cover surface, the film's refractive index and thickness cause a measurable increase in reflected light, as shown in **Figure 1B**. This reflected signal can be captured by a position-sensitive detector (e.g., CCD camera), enabling visualization of the film's morphology.

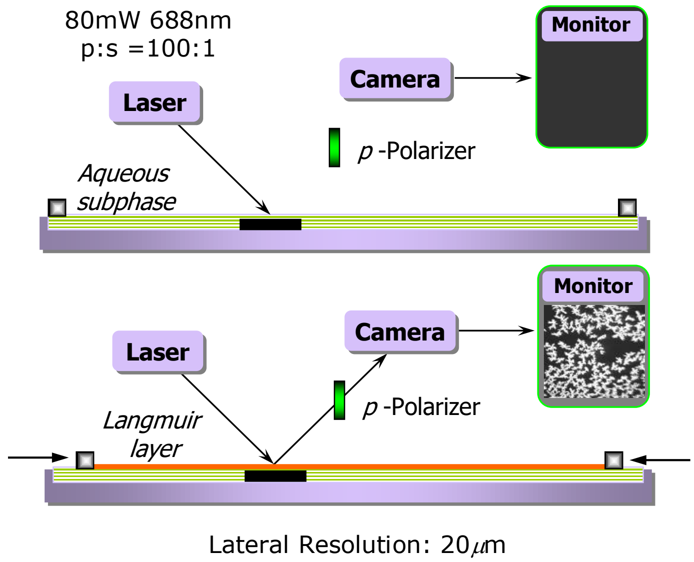

Figure 2. Schematic diagrams of BAM setup for a pure water surface (top) and a film covered surface (bottom) [9].

Figure 2 is a schematic diagram of a Mini-BAM experimental set-up, which includes a *p*-polarized diode laser source (688 nm), a *p*-polarizer, a CCD camera, and a Teflon trough [9]. The Mini-BAM differs from a traditional BAM mainly in where the polarizer is placed. In the Mini-BAM, the *p*-polarizer is positioned in the reflected-light path so that any residual *s*-polarized light is removed before reaching the detector. In a traditional BAM, the polarizer is placed in the incident-light path to filter out the *s*-component before the beam hits the surface. Filtering the reflected beam rather than the incoming beam enhances BAM image resolution [9]. The contrast seen in BAM images of Langmuir films comes from the differences in refractive index or film thickness between coexisting phases, such as gas, liquid-expanded, liquid-condensed, and solid states. BAM is usually more sensitive to changes in thickness than to refractive-index differences. For mixed monolayers, both refractive-index differences and thickness variations contribute to the observed contrast [2,3].

Module II. Machine Learning Workflow.

A machine learning-based image enhancement approach derived from Real-ESRGAN was employed to process BAM images in this study. The ML-based processing was implemented to improve image quality prior to subsequent image segmentation and quantitative domain analysis. The enhancement framework is based on a generative adversarial network (GAN), in which the generator follows an ESRGAN-style architecture composed of multiple Residual-in-Residual Dense Blocks (RRDBs), enabling effective extraction of hierarchical spatial features while maintaining stable image reconstruction [8,10].

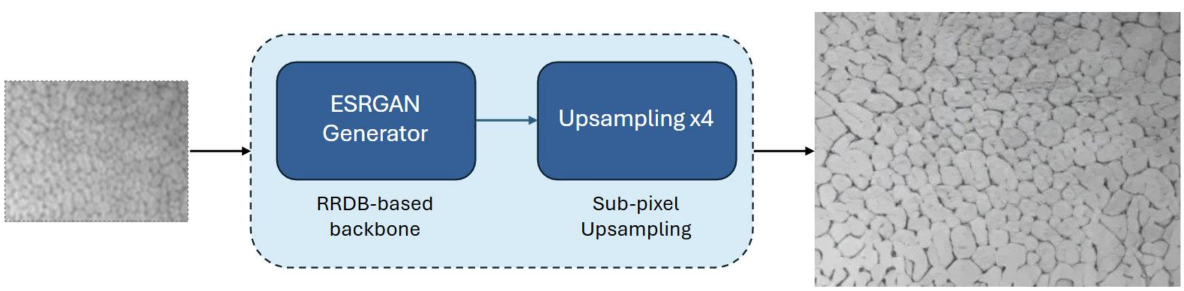

Figure 3. Schematic description pf Real-ESRGAN-based image super-resolution workflow. Raw BAM images are processed by an ESRGAN-style generator with an RRDB-based backbone followed by 4 × sub-pixel upsampling to suppress noise, enhance contrast and improve domain boundary visibility.

Figure 3 presents a schematic description of the Real-ESRGAN-based image super-resolution workflow. Raw BAM images are first provided as input to the RRDB-based generator, where feature maps are extracted and reconstructed through a series of convolutional layers. The generator output is subsequently upsampled by a factor of 4× using sub-pixel convolution (pixelshuffle) upsampling, which rearranges channel-wise feature representations into the spatial domain to enhance spatial resolution and visual clarity [11]. For this work, a pretrained Real-ESRGAN model was applied directly to raw BAM images without additional model retraining or the use of paired high-resolution ground truth images. At the pixel level, the enhancement process modifies local intensity distributions by leveraging spatial context learned during training. Rather than performing uniform or global pixel averaging, the network applies spatially adaptive intensity reconstruction, in which pixel values are recalculated based on the statistical features of their surrounding neighborhoods captured by deep convolutional filters [8].

Module III. MATLAB Image Analysis Workflow.

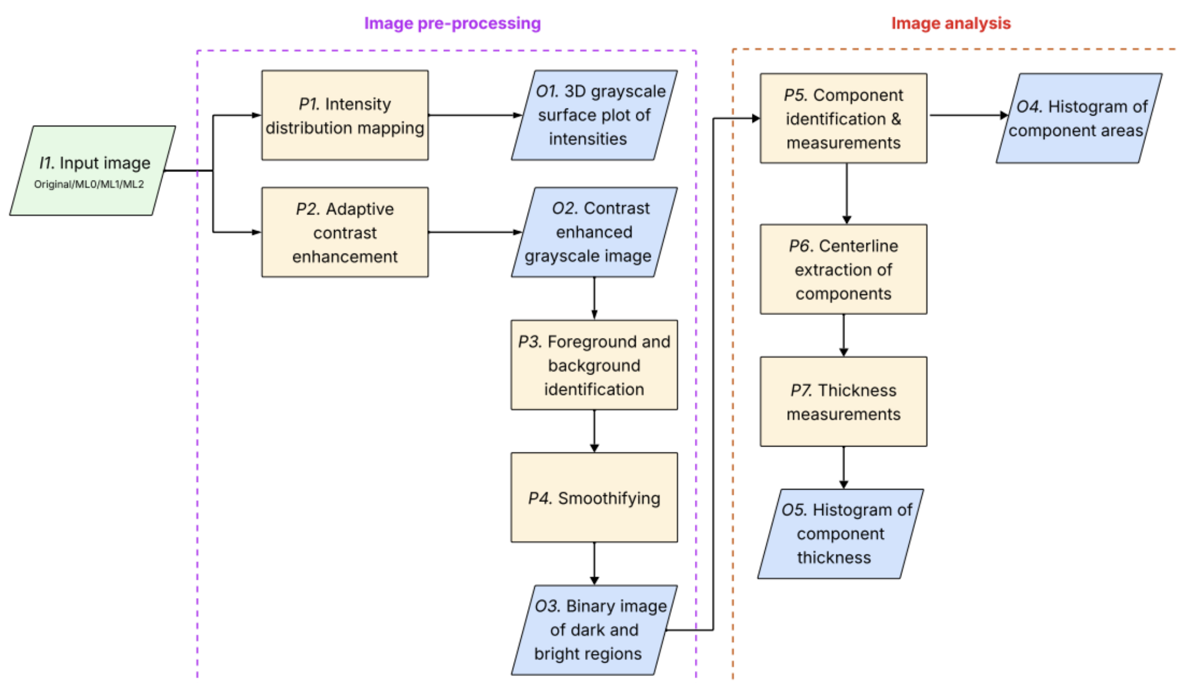

Figure 4. Schematic overview of the MATLAB image-processing and analysis workflow that begins with the input image, followed by a series of sequential image-processing and analysis steps that produce visual and quantitative data outputs.

The image analysis workflow begins with an input image (I1), which is used for both visual quality inspection and quantitative analysis [12]. The workflow shown in **Figure 4** is organized into two major components: Image Preprocessing and Image Analysis, with arrows indicating the direction of data flow through each step. Steps P1-P4 (shown in the light-yellow boxes) represent the pre-processing operations applied to both the raw and ML-processed BAM images. These steps are executed to enhance image quality and prepare the data at pixel level for subsequent quantitative analysis. The corresponding outputs O1-O3 are 3D grayscale intensity surface plots (O1), contrast enhanced grayscale images (O2), and binary black and white images (O3), respectively. These intermediate outputs serve as the inputs for the Image Analysis procedure shown in steps P5-P7, enabling quantitative domain assessment, including the numbers (if applicable), area, and average thickness for domains identified within each segmented BAM images. The measurement results thus obtained were summarized in histogram outputs (O4 and O5), which were included in the result section of this paper for further discussion.

Results and Discussion

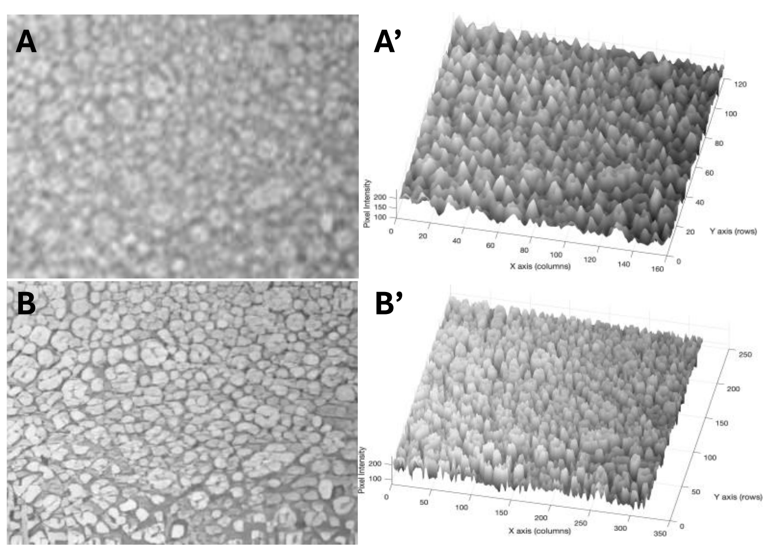

Figure 5. (A) Raw and (B) ML-processed BAM images obtained at 22.5 °C and a compression rate of 20 $cm^2 \cdot min^{-1}$ during 1st compression stage for a PCL/o-PS blend with $X_{PS} \sim 0.68$. The raw BAM image was taken at a surface of ~11 $Å^2 \cdot monomer^{-1}$, near the onset of unstable regime

of the Langmuir film. The BAM images are 1.6×1.2 mm^2 in size. (A') and (B') are 3D intensity surface plots (O1) processed from raw (A) and processed (B) BAM images, respectively.

Figure 5 shows the raw and ML-processed BAM images for an immiscible PCL/o-PS Langmuir films with oligomeric PS mole fraction of $X_{PS} \sim 0.68$. The raw image was captured near the onset of unstable regime, where de-mixing process takes place. By looking at **Figure 5A**, BAM clearly captured the spherical domains with enhanced brightness, indicating that this stage of phase separation is governed by a nucleation and growth mechanism. It is worth noting that the brightness in BAM image in **Figure 5A** does not arise from height variations of domains formed at the A/W interface. Instead, the observed contrast is attributed to the differences in the refractive index relevant to water subphase between the two phase separated regions (i.e., PS-rich vs PCL-rich regions) in the surface films. For BAM technology, a higher refractive index relative to the water subphase produces stronger reflectivity, correlated to brighter pixel intensity. Since PS has a significantly higher refractive index (1.59) than that of PCL (1.48), PS-rich domains generate more optical contrast relative to the water surface and therefore appear brighter than that of PCL-rich phase, This suggest that the brighter spherical domains on **Figure 5A** are PS-rich phase, while the darker areas around the brighter domains are PCL-rich regions, which were evolved during the de-mixing process of the mixed films upon dynamic compression.

Figure 5B, an ML-processed BAM image of **Figure 5A**, shows that the brighter PS-rich domains appear noticeably flattened compared to those in the raw BAM images. Within optically uniform regions (e.g., visually bright flat domains), neighboring pixel intensities tend to be averaged in a context-aware manner, resulting in reduced background noise and flattened intensity variations. In contrast, near domain boundaries, intensity gradients are selectively preserved or enhanced due to boundary-aware feature reconstruction learned through adversarial training [13]. Therefore, the phase boundaries between the two phases are significantly sharpened, resulting in more well-defined phase separated surface morphology with enhanced boundaries. In addition, the use of sub-pixel convolution ensures that newly generated pixels are reconstructed from learned feature maps rather than simple interpolation, leading to physically consistent redistribution of pixel intensities at the sub-domain scale.

Figure 5A' and **5B'** show the 3D surface plots of image intensity data, generated as output images (O1) using MATLAB's *surf* function, as outlined in the workflow in **Figure 3.** For instance, each pixel in **Figure 5A** is represented in a 3D coordinate $(x, y, z) =$ $(\text{column index, row index, pixel intensity})$ in **Figure 5A'**, with z-axis corresponding to the pixel intensity (brightness), instead of height. By comparing **Figure 5A'** and **5B'**, the intensity peak regions appear truncated in the surface plot for the ML-processed image in comparison to that for the raw image. The observation can be attributed to the pixel-level reconstruction mechanism of the Real-ESRGAN–based enhancement framework [8]. Rather than preserving absolute pixel intensity values from the raw BAM images, the network recalculates pixel intensities based on learned spatial correlations within local neighborhoods. This process effectively suppresses high-frequency fluctuations and redistributes pixel brightness in a spatially adaptive manner.

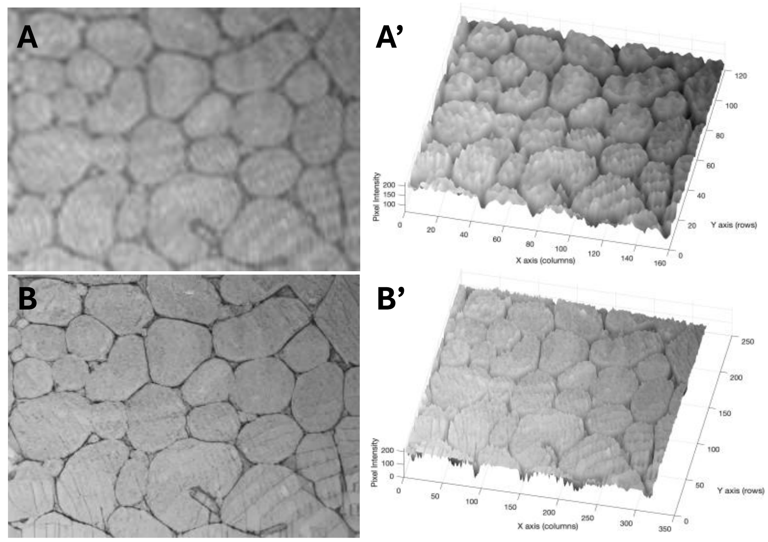

Figure 6. (A) Raw and (B) ML-processed BAM images obtained at 22.5 °C and a compression rate of 20 $cm^2 \cdot min^{-1}$ during 1st compression stage for a PCL/o-PS blend with $X_{PS} \sim 0.68$. The raw BAM image was taken at a surface area of ~10.4 $Å^2 \cdot monomer^{-1}$ in the unstable regime of the Langmuir film. The BAM images are 1.6 × 1.2 mm^2 in size. (A’) and (B’) are 3D intensity surface plots (O1) processed from raw (A) and processed (B) BAM images, respectively.

BAM images for the PCL/o-PS Langmuir films of $X_{PS} \sim 0.68$ were also captured at a surface area of ~10.4 $Å^2 \cdot monomer^{-1}$ and ~ 9.8 $Å^2 \cdot monomer^{-1}$, corresponding to **Figure 6A** and **Figure 7A**, respectively. A lower surface area per monomer corresponding to a higher surface pressure promotes phase separation in the PCL/o-PS blends and drives the growth of PS-rich domains, ultimately causing smaller domains to coalesce into larger ones, as shown in **Figure 6A** in comparison to those in **Figure 5A**. Upon further compressing the film to a surface area of ~ 9.8 $Å^2 \cdot monomer^{-1}$, spherical PS-rich domains captured in **Figure 6A** continue to grow by coarsening into larger domains, resulting in a nearly bi-continuous morphology, as shown in **Figure 7A**. Both **Figure 6A** and **7A** suggest the PS-rich domains display flat features by visual assessment. It is worth noting that this suggests that the PS distribution within the bright domains is uniform, as the contrast in brightness in these BAM images primarily arises from the refractive index contrast between PCL-rich and PS-rich phases. The domain brightness appears more uniform in **Figures 6A** and **7A** compared with that in **Figure 5A**, further suggesting that the de-mixing process between the two phases is more advanced when the Langmuir film is compressed to higher surface-pressure regimes.

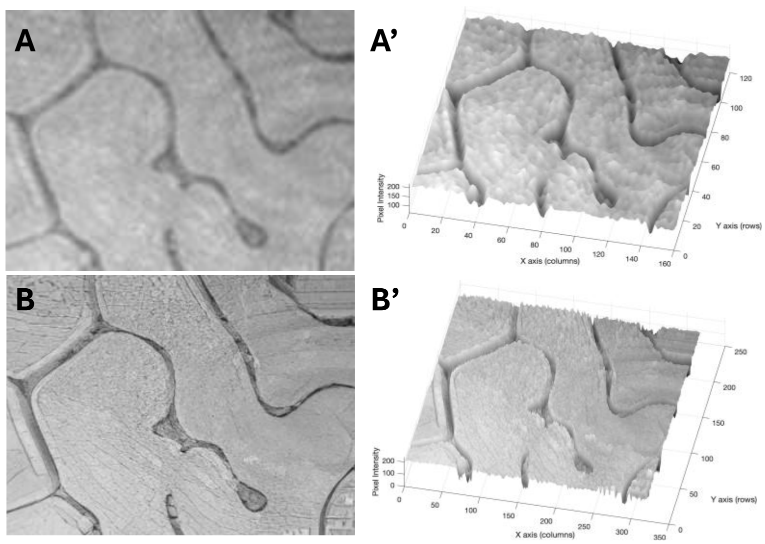

Figure 7. (A) Raw and (B) ML-processed BAM images obtained at 22.5 °C and a compression rate of 20 $cm^2 \cdot min^{-1}$ during 1st compression stage for a PCL/o-PS blend with $X_{PS} \sim 0.68$. The raw BAM image was taken at a surface area of ~ 9.8 $Å^2 \cdot monomer^{-1}$ in the unstable regime of the Langmuir film. The BAM images are 1.6×1.2 mm^2 in size. (A’) and (B’) are 3D intensity surface plots (O1) processed from raw (A) and processed (B) BAM images, respectively.

The 3D intensity plots were also generated for raw BAM images in **Figures 6A** and **7A** and their ML-process counterparts. For raw BAM images, the brightness of PS-rich domains appears significantly more uniform in pixel intensity (see **Figure 6A’** and **7A’**) in comparison to that for **Figure 5A’**, further demonstrating that as the de-mixing process progresses, the PS-rich domains not only grow in size but also evolve into a more compositionally uniform phase. The

ML-processed images (**Figure 6B** and **7B)** exhibit well-defined phase-separated morphology with sharp boundaries. Meanwhile, it was also noted that some small, finer secondary domains (which appear brighter within the PS-rich domains) are visible in **Figures 6A'** and **7A'** but diminished in **Figures 6B'** and **7B'.**

For optically uniform, quasi-2D domains such as those observed in the $X_{PS} \sim 0.68$ samples, the adaptive reconstruction of the Real-ESRGAN–based workflow leads to averaging of pixel intensities within individual domains, resulting in flattened intensity plateaus in the corresponding 3D grayscale surface plots. Meanwhile, intensity gradients at phase boundaries are preserved or moderately enhanced due to the network's sensitivity to edge-related features learned during adversarial training. As a result, the ML-processed images exhibit reduced variation in intra-domain intensity while maintaining well-defined domain boundaries. It is important to note that the reduced intensity variation seen in the ML-processed images does not represent the actual height or thickness distribution of the Langmuir films. Instead, the observed flattening effect arises from the redistribution of pixel intensities during image reconstruction. Although this effect may reduce how clearly fine heterogeneous domains can be visualized, it can clear the boundaries and prepare the images for segmentation-based measurements.

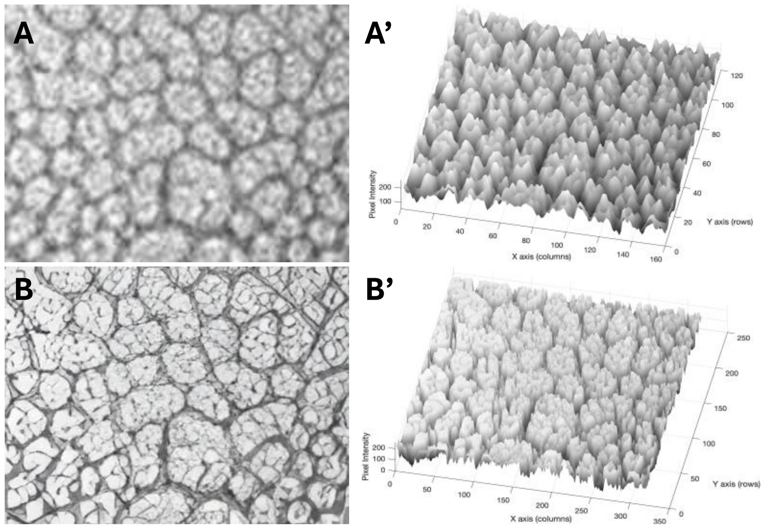

Figure 8. (A) Raw and (B) ML-processed BAM images obtained at 22.5 °C and a compression rate of 20 $cm^2 \cdot min^{-1}$ during 1st compression stage for a PCL/o-PS blend with $X_{PS} \sim 0.77$. The raw BAM image was taken at a surface area of ~ 7.3 $Å^2 \cdot monomer^{-1}$ in the unstable regime of the Langmuir film. The BAM images are 1.6×1.2 mm^2 in size. (A’) and (B’) are 3D intensity surface plots (O1) processed from raw (A) and processed (B) BAM images, respectively.

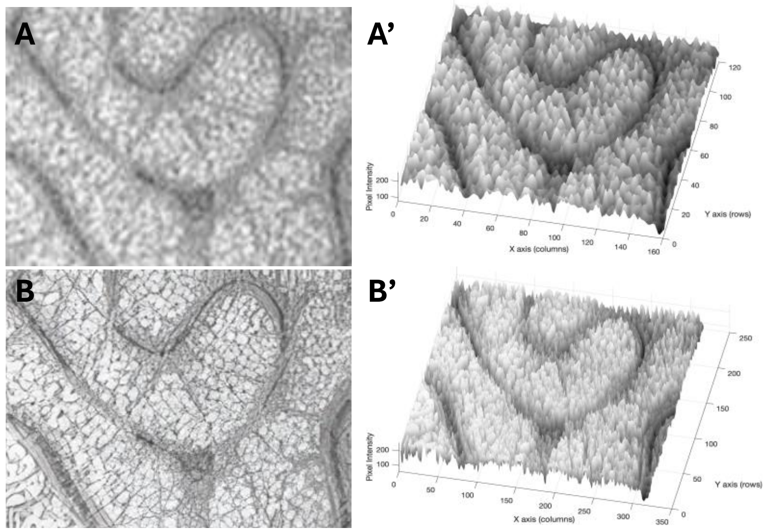

Figure 9. (A) Raw and (B) ML-processed BAM images obtained at 22.5 °C and a compression rate of 20 $cm^2 \cdot min^{-1}$ during 1st compression stage for a PCL/o-PS blend with $X_{PS} \sim 0.77$. The raw BAM image was taken at a surface area of ~ 6.1 $Å^2 \cdot monomer^{-1}$ in the unstable regime of the Langmuir film. The BAM images are 1.6×1.2 mm^2 in size. (A’) and (B’) are 3D intensity surface plots (O1) processed from raw (A) and processed (B) BAM images, respectively

To further assess the image enhancing capacity of the Real-ESRGAN–based workflow, BAM images taken for a PCL/o-PS mixed film of $X_{PS} \sim 0.77$ were also processed and the results were shown in **Figure 8** and **9** respectively. Both **Figure 8A** and **9A** were selected because they display more pronounced fine secondary domains within the larger domains, helping to resolve the visual ambiguity in related to secondary-domain features that are present in F**igure 5A**. For instance, the ML-processed images in **Figure 8B** clearly isolated small secondary bright domains within the spherical domains, while the ML algorithm still flattened the pixel intensity of these finer domains, which was further evidenced by the 3D intensity plot in **Figure 8’**. In addition, the ML-processed BAM images in **Figures 7B** and **8B** clearly reveal three distinct brightness levels corresponding to the bright white regions, grey regions, and dark regions, corresponding to

PS-rich multilayer aggregates (bright white regions) on top of the PS-rich monolayers (the large domains that appear as the grey background), and the dark regions correspond to PCL-rich areas that were de-mixed from the PS phase. The processed $X_{PS} \sim 0.77$ images clearly show that the Real-ESRGAN workflow can resolve and isolate secondary heterogeneous domains within primary domains while sharpening boundaries, effectively preparing the images for subsequent segmentation analysis.

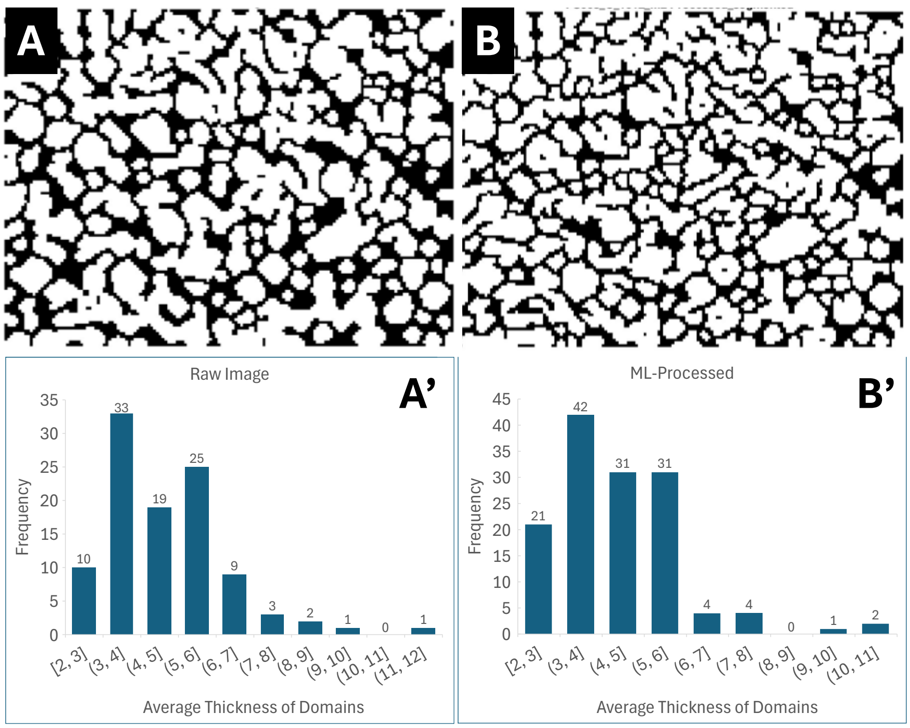

Figure 10. Segmented (A) raw and (B) ML-processed BAM images prepared for domain identification and thickness analysis. Binary black and white images **Figure 9A** and **9B** correspond to raw and ML-process BAM images in **Figure 5A** and **5B**. The images are 1.6 × 1.2 mm^2 in size. (A') and (B') are histograms for domain thickness extracted from segmented images in (A) and (B), respectively.

Binary black and white images presented in **Figure 10A** and **10B** are segmented raw and ML-process BAM images displayed in **Figure 5A** and **5B**, respectively. To obtain segmented images, MATLAB's *adapthisteq* function was first applied to an input image (i.e., I1 in the workflow chart in **Figure 4**) to perform adaptive histogram equalization (P2), which enhances local contrasts and produces an output grayscale image (O2) with sharped edges and improved texture visibility. The contrast-enhanced grayscale image (O2) was then processed as an input to perform foreground-background separation (P3) using MATLAB's *kmeans* clustering algorithm with $k = 2$ and five replicates, followed by image smoothing (P4) using *bwmorph* function. The outputs are binary segmented images (O3) shown in **Figure 10A** and **10B**.

Overall, the segmentation process isolates and separates the bright domain structures from the background of the image, so the number and size of the domains can be measured by following steps P5-P7 (**Figure 4**). Based on visual inspection, the segmented ML-processed image displays a greater number of smaller domains compared with that for raw BAM image, indicating that the chosen ML algorithm can isolate smaller features by sharpening and cleaning the phase boundaries. The output histograms (O5) produced for segmented images are shown in **Figure 10A'** and **10B'**, respectively. The average thickness measurements, expressed in pixels, further show that average domain thickness shifts toward lower value for the segmented ML-processed images, which is consistent with the visual observations.

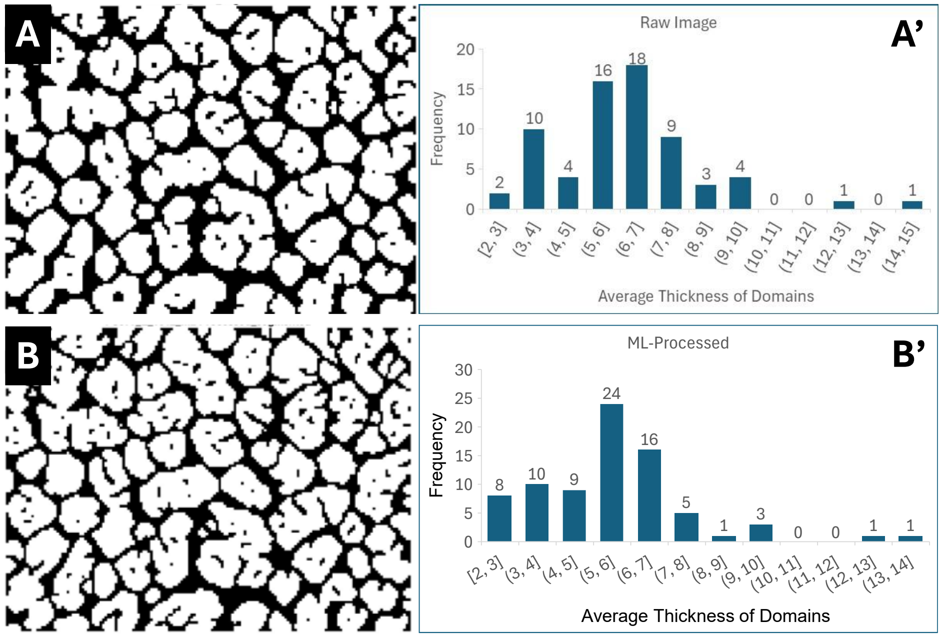

Figure 11. Segmented (A) raw and (B) ML-processed BAM images prepared for domain identification and thickness analysis. **Figure 11** (A) and (B) correspond to raw and ML-process images in Figure 8. The raw image was obtained at 22.5 °C and a compression rate of 20 $cm^2 \cdot min^{-1}$ during 1st compression stage for a PCL/o-PS blend with $X_{PS} \sim 0.77$. The raw BAM image was taken at a surface of ~ 7.3 $Å^2 \cdot monomer^{-1}$ in the unstable regime of the Langmuir film. The images are 1.6 × 1.2 mm^2 in size. (A') and (B') are histograms for domain thickness extracted from raw segmented images in (A) and (B), respectively.

Above-mentioned segmentation process was also carried out for the raw and ML-process BAM images that show visible small secondary domains (see **Figure 8A** and **8B**). The segmented images and their corresponding average-domain-thickness histograms are presented in **Figure 11**. By visual inspection of the segmented ML-processed images (**Figure 11B**), the spherical PS-rich domains that grow through a nucleation and growth mechanism are subdivided into smaller sections, reflecting small secondary domains grown within the spherical structures as seen in the raw BAM image (**Figure 8A**). In contrast, far fewer secondary domain features are captured in the segmented raw BAM image (**Figure 11A**) compared with that for the ML-processed image. Consequently, the average domain thickness values also shift toward lower levels in the segmented ML-processed images. Overall, **Figures 10** and **11** provide clear evidence that the ML-processed BAM images enable more effective identification of smaller domains and clearer delineation of phase boundaries, contributing meaningfully to improved segmentation analysis. Segmentation and measurements were also carried out for **Figures 9A** and **9B**, which also display secondary structures within the primary large bi-continuous domains. The same trend was observed, and the results are summarized in **Table 1**.

Table 1. Summary of the number of isolated domains, their areas, and their average thickness for segmented BAM images containing fine secondary domain structures.

Figure #	**Figure 5A, 5B**		**Figure 8A, 8B**		**Figure 9A, 9B**	
	Orig.	ML-Proc.	Orig.	ML-Proc.	Orig.	ML-Proc.
# of Domains	103	136	68	78	55	66
Area (Mean)	119.9	94.2	187.2	168.6	218.8	183.6
Thickness (Mean)	5.1	4.5	6.4	5.6	4.3	4.1

Conclusions

An advanced machine learning workflow via a Real-ESRGAN–based generative deep learning framework was performed for the first time to denoise, enhance, and prepare BAM images for subsequent quantitative analysis using MATLAB. Characteristic BAM images selected for this study included (1) spherical and bi-continuous surface morphologies formed through either nucleation and growth or spinodal decomposition mechanisms, and (2) optically uniform domains and optically heterogeneous domains containing secondary structures within the domains. Key findings of the study are summarized as follows:

Visual assessment of all raw and ML-processed images, regardless of their morphological characteristics, demonstrates that the ML-enhanced images exhibit substantially higher optical contrast and cleaner boundaries between PS-rich domains and PCL-rich phase. For images containing optically uniform domains (i.e., $X_{PS} \sim 0.68$ samples), the network performs spatially adaptive intensity averaging within local neighborhoods, effectively reducing random noise while preserving coherent domain structures. As a result, the overall intensity distribution within PS-rich domains remains largely unchanged, while phase boundaries are sharpened through boundary-aware feature reconstruction. While for heterogeneous domains containing secondary features with higher optical intensity (i.e., $X_{PS} \sim 0.77$ samples), the learned averaging behavior of the network may partially suppress localized intensity extrema, a behavior commonly observed in blind super-resolution models trained to optimize perceptual consistency [8,14], and consistent with the perception-distortion tradeoff inherent in GAN-based reconstruction methods [15]. This effect arises because the pretrained model is optimized to restore visually consistent textures rather than preserve isolated high-intensity features that deviate from dominant spatial patterns [8]. Consequently, while the boundaries of those small secondary domains are preserved, small brighter domains may appear smoothened (i.e., pixel intensity being averaged) in the ML-processed images.

Segmentation analysis results (summarized in **Table 1**) demonstrate promising performance of the Real-ESRGAN logarithm to prepare images for segmentation and quantitative domain analysis. A greater number of small domains that are visible in the raw BAM images can be isolated in the segmented ML-processed images compared with that in the segmented raw images. The same trend was also observed for all BAM images containing secondary PS-rich domains (brightest phase in the raw images) within the primary PS-rich domains, regardless of whether the primary domains evolved through nucleation and growth (**Figures 5** and **8**) or spinodal decomposition mechanisms (**Figure 9**). Despite the limitations of the Real-ESRGAN framework, the ML-enhanced images provide improved grouping of pixel intensities, enabling clearer differentiation among multilayer PS aggregates, PS-rich monolayer domains, and the PCL-rich phase. This improved intensity consistency supports more reliable segmentation and quantitative analysis, confirming the hypothesized phase separation behavior in mixed polymer Langmuir films.

The observed suppression of localized intensity extrema in the ML-processed images should not be interpreted as algorithm-induced artifacts. Instead, this behavior reflects a fundamental perception-distortion tradeoff inherent in GAN-based image reconstruction methods, where improvements in visual consistency and structural interpretability are achieved at the expense of preserving absolute pixel-level intensity variations [15]. Future improvements may be achieved by retraining or fine-tuning the model using domain-specific BAM image datasets, particularly those containing pronounced 3D features and heterogeneous intensity distributions. Incorporating microscopy-specific degradation models and loss functions that emphasize the preservation of localized intensity variations may further enhance the fidelity of ML-processed images while maintaining segmentation performance.

Overall, considering the limitations of BAM technology and its importance for interpreting the complex *in-situ* morphology of Langmuir films, the above findings presented in this study become particularly promising, as it enables an AI-driven transition from traditional qualitative observations to a more quantitative study of quasi-2D phase behavior of polymers and other surface-active materials. Furthermore, this study not only demonstrates the value of AI in addressing a specific research problem but also shows how a modular learning and research model can support interdisciplinary collaboration on AI integration. As AI technology evolves rapidly, many institutions struggle to keep pace, which further widens the gap between resource-abundant and resource-scarce institutions. These disparities influence students' career readiness, faculty research productivity, as well as funding opportunities. We foresee that this modular learning and research strategy can be readily adapted into an interdisciplinary, experiential learning course in different institutions. Participating faculty can co-design and co-teach the course, helping integrate AI more effectively into both learning and research workflows.

References

[1] J. J. Giner-Casares, G. Brezesinski, and H. Möhwald, "Langmuir monolayers as unique physical models," Current Opinion in Colloid & Interface Science, vol. 19 (3), pp.176-182, 2014.

[2] B. Li, H. Marand, and A. R. Esker, "Dendritic growth of poly(ε-caprolactone) crystals from compatible blends with poly(t-butyl acrylate) at the air/water interface", Journal of Polymer Sciences B: Polymer Physics, vol. 45 (24), pp. 3200-3318, 2007.

[3] B. Li, A. R. Esker, "Blends of Poly(ε-caprolactone) and Intermediate Molar Mass Polystyrene as Langmuir Films at the Air/Water Interface", Langmuir 2007, vol. 23 (2), pp. 574-581, 2007.

[4] B. Li, Y. Wu, M. Liu, and A. R. Esker, "Brewster angle microscopy study of poly(ε-caprolactone) crystal growth in Langmuir films at the air/water Interface", Langmuir, vol.22 (11), pp. 4902-4905, 2006.

[5] B. Li, A. R. Esker, "Molar mass dependent growth of poly(ε-caprolactone) crystals in Langmuir films", Langmuir, vol. 23(5), 2546-2554, 2007.

[6] B. Li and A. Esker, “Interface-modulated morphological transition of biodegradable poly(ε-caprolactone) crystals”, RSC Applied Interface, vol. 1, pp. 671-676, 2024.

[7] Q. Xie, B. Li, A. R. Esker, “Phase behavior of poly (ε-caprolactone)-b-poly (tert-butyl acrylate) block copolymer at the air/water interface,” Colloids and Surfaces A: Physicochemical and Engineering Aspects vol. 587, 124346, 2020.

[8] X. Wang, L. Xie, C. Dong and Y. Shan, "Real-ESRGAN: Training Real-World Blind Super-Resolution with Pure Synthetic Data," 2021 IEEE/CVF International Conference on Computer Vision Workshops (ICCVW), Montreal, BC, Canada, pp. 1905-1914, 2021.

[9] B. Li, “Phase behavior of poly(caprolactone) based polymer blends as Langmuir films at the air/water interface,” PhD dissertation, Virginia Tech, 2007.

[10] Wang, X., Xie, L., Dong, C., & Shan, Y., “Real-ESRGAN: Training real-world blind super-resolution with pure synthetic data,” In Proceedings of the IEEE/CVF international conference on computer vision, pp. 1905-1914, 2021.

[11] W. Shi et al., "Real-Time Single Image and Video Super-Resolution Using an Efficient Sub-Pixel Convolutional Neural Network," 2016 IEEE Conference on Computer Vision and Pattern Recognition (CVPR), Las Vegas, NV, USA, 2016, pp. 1874-1883, doi: 10.1109/CVPR.2016.207.

[12] Image Processing Toolbox, https://www.mathworks.com/help/images/index.html, published by MathWorks, 2023.

[13] C. Ledig et al., “Photo-Realistic Single Image Super-Resolution Using a Generative Adversarial Network," 2017 IEEE Conference on Computer Vision and Pattern Recognition (CVPR), Honolulu, HI, USA, 2017, pp. 105-114, 2017.

[14] X. Wang et al., “ESRGAN: Enhanced super-resolution generative adversarial networks,” In Proceedings of the European conference on computer vision (ECCV) workshops, 2018.

[15] Y. Blau, T. Michaeli, “The perception-distortion tradeoff,” In Proceedings of the IEEE conference on computer vision and pattern recognition, pp. 6228-6237, 2018.